

INFRARED FABRY-PEROT IMAGING OF M82 [Fe II] EMISSION. II. TRACING EXTRAGALACTIC SUPERNOVA REMNANTS

MATTHEW A. GREENHOUSE,¹ SHOBITA SATYAPAL,^{1,2} CHARLES E. WOODWARD,^{3,4}
 J. FISCHER,⁵ K. L. THOMPSON,⁶ W. J. FORREST,² J. L. PIPHER,² N. RAINES,²
 H. A. SMITH,¹ D. M. WATSON,² AND R. J. RUDY⁷

Received 1996 March 25; accepted 1996 August 23

ABSTRACT

We report high spatial and spectral resolution [Fe II] 1.644 μm Fabry-Perot imaging observations of M82. We present extinction-corrected [Fe II] images and discuss the nature of compact [Fe II] emission regions revealed by these new data. We conclude that these [Fe II] sources trace a population of supernova remnants in M82 that are substantially older than those revealed previously on 6 cm radiographs. In addition, we find that M82 contains a distributed [Fe II] emission component that is extended along the southern minor axis and that accounts for 90% of the galaxy's [Fe II] luminosity. We interpret this extended emission as tracing disk material entrained in a super wind that has broken out of the galactic disk to the south. We find that the [Fe II]/Br γ line ratio throughout M82 correlates with the age of the starburst as reflected by the color of the photospheric emission from the galaxy's stars. This correlation suggests that the [Fe II] emission regions in M82 are colocated with a post-main-sequence stellar population. The engineering details of our Fabry-Perot imaging methodology are also discussed.

Subject headings: galaxies: individual (M82) — galaxies: stellar content — galaxies: structure — infrared: galaxies — supernova remnants — techniques: interferometric

1. INTRODUCTION

The possibility that infrared [Fe II] emission can reveal the supernova activity of galaxies has stimulated increasing observational work over the past few years. Issues surrounding [Fe II] as a tracer of supernova remnants in galaxies via grain processing were discussed by Greenhouse et al. (1991), hereafter Paper I. Since that time, other interpretations of [Fe II] emission have been proposed (Mouri, Kawara, & Taniguchi 1993), progress has been made in understanding relationships between infrared [Fe II] lines and other emission components (e.g., Forbes & Ward 1993; Colina 1993; Lumsden & Puxley 1995), new imaging spectrophotometry of [Fe II] in nearby galaxies has been obtained (Forbes et al. 1993; Moorwood & Oliva 1994; van der Werf et al. 1993; Blietz et al. 1994), and new calculations of Fe⁺ energy levels and collisional excitation rate coefficients have been produced (Pradhan & Zang 1993; Zang & Pradhan 1995; Nahar 1995).

Emission-line imaging of nearby galaxies has revealed two categories of near-infrared [Fe II] emission: (1) a distributed, uniform [Fe II] background emission and also (2) compact [Fe II] sources. The distributed emission has been seen to correlate spatially with global nuclear outflows such as starburst super winds or active galactic nucleus radio jets. The compact [Fe II] sources often show weak or no spatial correlation with other infrared line emission such as

H₂, H I, [Ne II], or continuum emission in the *K* band or at 6 cm.

The near-infrared [Fe II] image data obtained to date consist of low spectral resolution narrowband filter images or low spatial resolution images assembled from long-slit spectra. In this paper, we present the first near-infrared [Fe II] Fabry-Perot images of a galaxy—a technique that yields both high spectral and high spatial resolution. In the following section, we discuss our methodology for Fabry-Perot imaging, the image analysis, and technical details of our M82 [Fe II] observations. In § 3, we discuss our Fabry-Perot images of M82 and new clues that they reveal about the origin of M82's [Fe II] emission.

2. OBSERVATIONS

2.1. Methodology: Prefiltering Facility Cameras with Fabry-Perot Imaging Systems

Recent advances in low noise detector arrays have made Fabry-Perot imaging an increasingly practical technique for moderate-resolution $\lambda/\Delta\lambda \simeq 10^3$ imaging spectroscopy at near-infrared wavelengths. High system accuracy and reliability can be achieved with commercially available etalons such as those produced by Queensgate Instruments LTD.⁸ Optimal optical coupling between the Fabry-Perot and camera subsystems is critical for acquisition of data on faint, extended objects such as galaxies and has not been adequately discussed in recent articles describing infrared Fabry-Perot imaging systems. As a consequence, we begin by briefly reviewing engineering details that govern the optical coupling of Fabry-Perot etalons to infrared cameras.⁹ Details of our M82 observations and data reduction are discussed in § 2.2.

In moderate spectral resolution infrared applications

¹ National Air and Space Museum, Laboratory for Astrophysics, Smithsonian Institution, Washington, DC 20560.

² Department of Physics and Astronomy, University of Rochester, Rochester, NY 14627-0011.

³ Department of Physics and Astronomy, University of Wyoming, Laramie, WY 82071.

⁴ Presidential Faculty Fellow, NSF.

⁵ Remote Sensing Division, Naval Research Laboratory, Code 7600, 4555 Overlook Avenue, SW, Washington, DC 20375.

⁶ Department of Astronomy, University of Texas, RLM 15.308, Austin, TX 78712.

⁷ The Aerospace Corporation, P.O. Box 92957, Los Angeles, CA 90009.

⁸ Queensgate Instruments LTD, Queensgate House, Waterside Park, Bracknell, RG12 1RB, England.

⁹ For a more complete treatment of Fabry-Perot formalism, we recommend Vaughan (1989) and Atherton et al. (1981).

Report Documentation Page				Form Approved OMB No. 0704-0188	
Public reporting burden for the collection of information is estimated to average 1 hour per response, including the time for reviewing instructions, searching existing data sources, gathering and maintaining the data needed, and completing and reviewing the collection of information. Send comments regarding this burden estimate or any other aspect of this collection of information, including suggestions for reducing this burden, to Washington Headquarters Services, Directorate for Information Operations and Reports, 1215 Jefferson Davis Highway, Suite 1204, Arlington VA 22202-4302. Respondents should be aware that notwithstanding any other provision of law, no person shall be subject to a penalty for failing to comply with a collection of information if it does not display a currently valid OMB control number.					
1. REPORT DATE 1997		2. REPORT TYPE		3. DATES COVERED 00-00-1997 to 00-00-1997	
4. TITLE AND SUBTITLE Infrared Fabry-Perot Imaging of the M82 [Fe II] Emission. II. Tracing Extragalactic Supernova Remnants				5a. CONTRACT NUMBER	
				5b. GRANT NUMBER	
				5c. PROGRAM ELEMENT NUMBER	
6. AUTHOR(S)				5d. PROJECT NUMBER	
				5e. TASK NUMBER	
				5f. WORK UNIT NUMBER	
7. PERFORMING ORGANIZATION NAME(S) AND ADDRESS(ES) Naval Research Laboratory, Code 7600, 4555 Overlook Avenue, SW, Washington, DC, 20375				8. PERFORMING ORGANIZATION REPORT NUMBER	
9. SPONSORING/MONITORING AGENCY NAME(S) AND ADDRESS(ES)				10. SPONSOR/MONITOR'S ACRONYM(S)	
				11. SPONSOR/MONITOR'S REPORT NUMBER(S)	
12. DISTRIBUTION/AVAILABILITY STATEMENT Approved for public release; distribution unlimited					
13. SUPPLEMENTARY NOTES					
14. ABSTRACT					
15. SUBJECT TERMS					
16. SECURITY CLASSIFICATION OF:			17. LIMITATION OF ABSTRACT	18. NUMBER OF PAGES 9	19a. NAME OF RESPONSIBLE PERSON
a. REPORT unclassified	b. ABSTRACT unclassified	c. THIS PAGE unclassified			

involving relatively high f-ratio ($\geq f/15$) telescopes, an optimal optical configuration for a Fabry-Perot camera system is one in which the etalons are located directly in the telescope beam. The standard alternative configuration incorporates collimating optics that add complexity, reflection, and transmission losses. When a Fabry-Perot is used directly in a converging or diverging beam of cone angle φ , its resolving power is limited to $R_{\text{beam}} = 8/\varphi^2$. The total system finesse is a quadrature sum of terms due to etalon plate reflectivity, defects of the plate parallelism and surface figure, as well as geometrical and diffraction optical defects on the incident beam. Optimal etalon transmission is achieved when the reflectivity finesse is much less than each defect finesse term. This condition can often be met at slow Cassegrain focal ratios without employing collimating optics. For example, an etalon with reflectivity finesse $N_r = 50$ operating in order $n = 20$ will have a resolving power of $R \equiv \lambda/\Delta\lambda \simeq nN_r = 10^3$. A $f/27$ telescope, such as the one used here (§ 2.2), yields $R_{\text{beam}} \simeq 5.8 \times 10^3 > R$ and a convergence defect finesse $N_{\text{beam}} = R_{\text{beam}}/n \simeq 290 > N_r$. The corresponding reduction in etalon transmission due to beam divergence is $1 - \tau_{\text{beam}} = 1 - (N_{\text{beam}}/N_r) \arctan(N_r/N_{\text{beam}}) = 0.01$. One can see that the collimating optics would afford no significant enhancement of this etalon's performance and would increase cost and complexity while reducing the system throughput as a result of reflection and transmission losses. The former loss can be particularly significant when the collimating optics must pass a broad wavelength range precluding the use of optimized anti-reflection coatings.

Unnecessary use of Fabry-Perot collimating optics can result in nonmonochromatic images that, in infrared applications, significantly increase observing time. For example, a Fabry-Perot transmission function has maxima given by $\lambda_0 = 2d \cos \theta/n$, where λ_0 is the wavelength of the n th order maxima, d is the effective gap length, and θ is the incidence angle of the chief ray from a point of interest in the object field. Chief rays arriving from field points across the field of view (FOV) differ in incidence angle by an amount that depends on the optics preceding the Fabry-Perot. This effect can be taken into account in image processing (§ 2.2) if, and only if, an image data cube is recorded over a sufficient number of gap settings to fully sample an emission line over the entire FOV.

In the near-infrared, the background emission due to OH airglow and/or thermal emission is generally bright and time variable on the scale of typical narrowband ($R = 10^3$), background-limited integration times ($\simeq 200$ s). As a result, explicit sky images must be obtained in concert with the object images at each gap setting. A sky-object-object-sky sequence is typically used to remove first-order temporal variations in the sky emission. Hence, in contrast to optical Fabry-Perot applications, each extra gap setting required by the above θ dependence results in at least four extra integrations. As a consequence, in infrared applications, it is critically necessary to minimize the range of chief ray incidence angles on the Fabry-Perot.

The range of incidence angles $\Delta\theta$ corresponding to a given FOV is often negligible when collimating optics are not used. In this case, $\Delta\theta = a/\psi$, where a is the field stop diameter, and ψ is the distance between the focal plane and the exit pupil of the telescope (for a Cassegrain telescope, $\psi = \text{primary mirror focal length} + \text{back focal distance}$, e.g., see Schroeder 1987). The focal length of a collimating

lens group that yields similar $\Delta\theta$ is often difficult and expensive to package, particularly in cryogenic applications.

2.2. M82 [Fe II] Observations and Data Reduction

In Paper I, we obtained small aperture ($2''.7$) grating spectra of two compact nonthermal continuum sources in M82. We speculated that high spatial resolution Fabry-Perot imaging could further reveal relationships between [Fe II] emission and supernova remnants in M82 and other galaxies. Here we report on Fabry-Perot imaging observations of the $a^4 D_{7/2} \rightarrow a^4 F_{9/2}$ ($1.644 \mu\text{m}$) Fe⁺ forbidden line in M82 obtained to further explore the origin of this emission.

The data were obtained with the NASM/NRL Fabry-Perot system and the University of Rochester Third Generation Camera at the Wyoming Infrared Observatory (WIRO) 2.34 m telescope ($f/27$) during 1991 May 12 UT. A single spatial position centered on the nucleus of M82 was observed using a 256^2 InSb SBRC focal plane array with a plate scale of $0''.25 \text{ pixel}^{-1}$. The spatial resolution was limited by seeing to $1''.3$ FWHM or 20 pc at the distance of M82 (3.2 Mpc; Tammann & Sandage 1968). All of the images shown here have been block averaged to a display scale of $0''.5 \text{ pixel}^{-1}$. Image rotation was determined at the telescope, and the images are shown here with pixel columns oriented north-south to within approximately $0''.1$. Coordinate axes are shown in units of arcseconds relative to the K-band nucleus: $\alpha(1950) = 9^{\text{h}}51^{\text{m}}43^{\text{s}}.47$, $\delta(1950) = 69^\circ55'00''.3$ (Pipher et al. 1987).

Four Fabry-Perot data cubes were obtained on the [Fe II] 1.644 line with a spectral resolution of 375 km s^{-1} . Each data cube consists of a three-dimensional image array (α, δ, z) , where α and δ are coordinates on the sky and z is proportional to the etalon gap length. The M82 data cubes consist of nine Fabry-Perot gap settings chosen to sample the line profile in steps of $(1/3)R$ and the underlying continuum at $(5/3)R$ on each side of line center. At each gap setting, four images were recorded following a standard sky-object-object-sky photometry sequence, thus yielding a total data set of 144 images. These images were individually linearized, flat-fielded, sky-subtracted, spatially registered, and calibrated using standard infrared image reduction techniques. Flux calibration was determined relative to the star BS 3888 (F0 IV). Spatial registration was determined by cross-correlation analysis on the point source K6 (Dietz et al. 1986), which is bright in [Fe II] and off-line continuum.

With the above reduction complete, the remaining task is to extract continuum-subtracted emission-line images and/or velocity maps from the processed data cubes. Two optical effects must be taken into account in this extraction: (1) the etalon plates typically have figure defects, and (2) the data cubes are curved because of the finite range of chief ray incidence angles $\Delta\theta$. Queensgate Instruments LTD model ET50WF etalons represent the state of the art in the near-infrared and consist of water-free, fused silica plates with reflective dielectric coatings. The coatings are applied at an elevated temperature, and a large number of layers are required to achieve broadband wavelength coverage. The expansion coefficient mismatch between the coating and the plate substrate produces a large surface stress upon cooling to room temperature, resulting in a bowl-shaped surface deformation. For near-infrared etalons with a fractional wavelength coverage of 0.25 and a clear aperture of 50 mm, the best commercially available etalons typically exhibit a

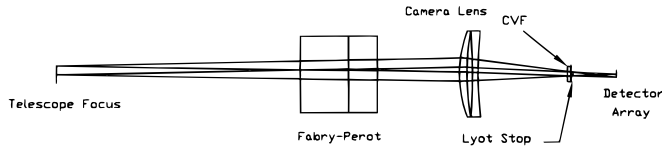


FIG. 1.—Optical layout of the Fabry-Perot camera system used here

flatness defect of at least 3 nm edge to center ($\lambda/200$ at $\lambda = 633$ nm), resulting in an etalon edge-to-center gap variation of roughly 6 nm.

For etalons used in a collimated beam, this gap variation reduces the effective finesse. However, in the optical configuration used here (Fig. 1), the radially symmetric deformation produces a radial dispersion across the array FOV.

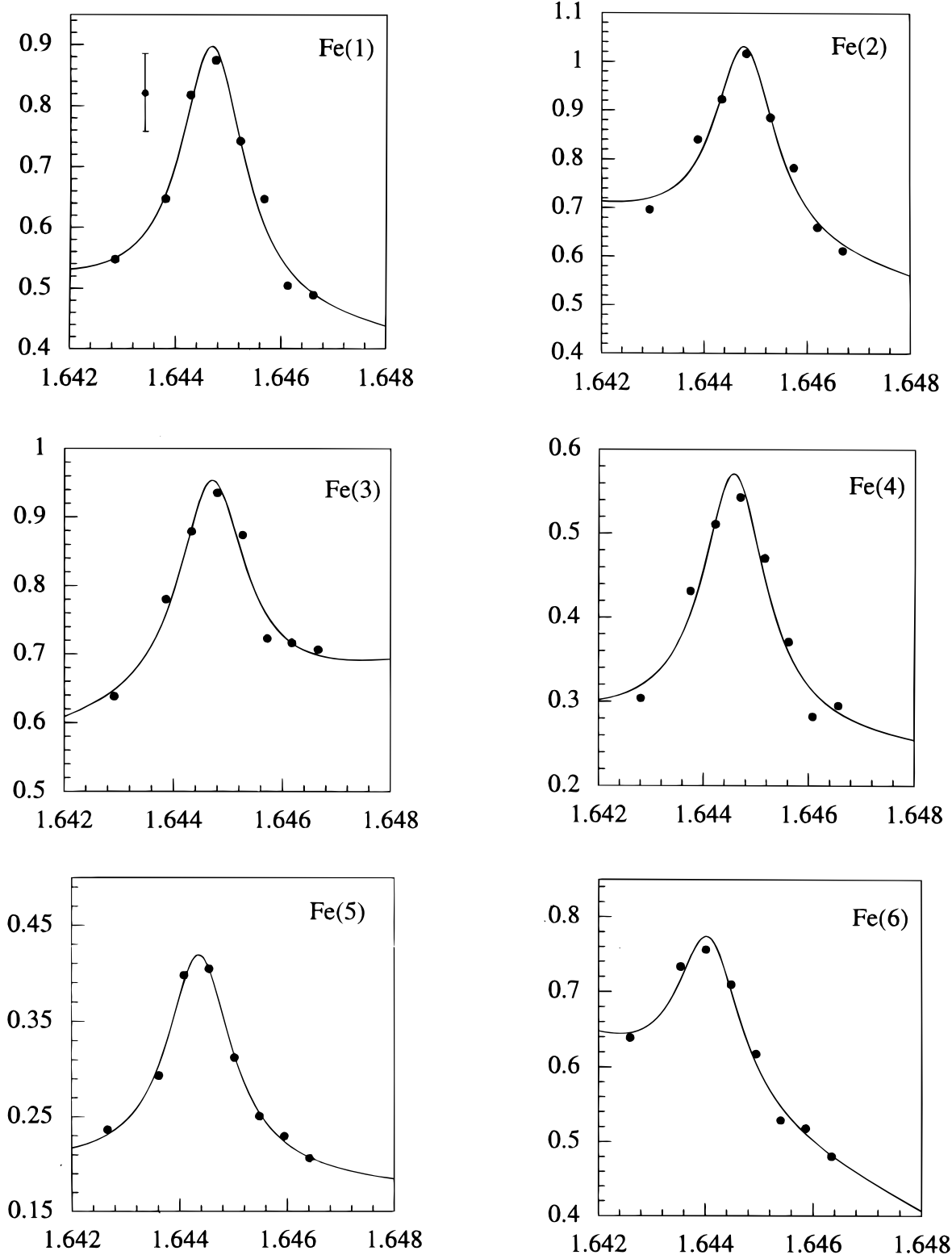


FIG. 2.—Spectra extracted from the Fabry-Perot data cubes described in § 2.2 at the spatial center of [Fe II] sources listed in Table 1. A typical 1σ error bar is shown in the upper left-hand corner of the top left panel.

TABLE 1
M82 [Fe II] 1.644 μ m COMPACT SOURCES

SOURCE	ASSOCIATION	OFFSETS FROM NUCLEUS ^a		FWHM ^b (pc)	A_V ^c	[Fe II] FLUX ^d		Pa β FLUX ^d		$N(\text{Fe}^+)^f$ $N(\text{H})$ (ppm)
		Fig. 4a (west, south)	Fig. 4b (west, south)			Observed	Intrinsic ^e	Observed	Intrinsic ^e	
Fe 1.....	...	4.2, 4.2	3.7, 3.3	43	9	12.5 ± 0.50	49.60	24 ± 2	189	2.36
Fe 2.....	...	6.5, 0.9	6.5, 0.9	37	9	8.55 ± 0.04	33.50	17 ± 2	147	1.37
Fe 3.....	...	11.2, 1.4	11.2, 1.4	22	6	2.49 ± 0.03	6.59	7.3 ± 0.1	39.6	1.50
Fe 4.....	10.2, 4.2	37	9	...	27.1	...	150	1.63
Fe 5.....	K5 ^g	23.7, 7.3	23.7, 7.3	22	...	1.57 ± 0.05	...	2.09 ± 0.4
Fe 6.....	K6 ^g	28.8, 10.2	28.8, 10.2	22	...	1.54 ± 0.06	...	2.4 ± 0.4

^a Offsets in arcseconds relative to $\alpha(1950) = 9^{\text{h}}51^{\text{m}}43^{\text{s}}.47$, $\delta(1950) = 69^{\circ}55'00''.3$.

^b FWHM source diameter.

^c Extinction data from Satyapal et al. (1995) averaged over listed source diameter.

^d $10^{-17} \text{ W m}^{-2}$ integrated over listed source diameter.

^e Corrected for extinction.

^f $[N(\text{Fe})/N(\text{H})]_{\odot} = 47 \text{ ppm}$ (Grevesse & Anders 1989).

^g Dietz et al. (1986).

The etalons used to obtain the observations reported here have a plate flatness of $\lambda/100$, yielding a wavelength shift of 1 nm between the center and the edge of the array FOV. As noted in § 2.1, a radial dispersion can also be introduced by the telescope optics. In the optical configuration of Figure 1, the detector array is the effective field stop $a = 11.3 \text{ mm}$, and at WIRO, $\psi = 5.89 \text{ m}$. Thus, $\Delta\theta = 0.002 \text{ rad}$, yielding a negligible wavelength shift.

At the telescope, we measure the actual shift due to the combination of these effects by obtaining data cubes on a monochromatic flat field produced by scattering discharge lamp light off of a diffusing screen. An Airy function is then fitted to the lamp line at each of 256^2 spatial pixels in the lamp data cube. The spatial variation of the effective etalon gap is thus measured, and the basis for a relative wavelength calibration of each spatial pixel in the astronomical data cubes is obtained. This procedure ensures that extraction of astronomical line images and velocity maps are not affected by the above optical effects. Absolute wavelength calibration is obtained by observation of lamp lines closely bracketing the astronomical line of interest and from OH airglow lines in the sky position data cubes.

The gap space data cubes (α, δ, z) are thus converted to wavelength space (α, δ, λ). A linear continuum baseline and line profile function are then fit to all of the data at each (α, δ). We typically use an Airy function convolved with a Gaussian as a profile-fitting function. If the width of the best-fit convolution exceeds the instrument-response function, a Gaussian deconvolution is performed to recover the true profile function of the emission line. However, in the case of M82, the [Fe II] emission was spectrally unresolved at all (α, δ) observed. Typical spectra extracted from the reduced data cubes on [Fe II] sources listed in Table 1 are shown in Figure 2.

At each pixel, a linear continuum baseline is subtracted, and the Gaussian line profile or the instrument-response function is integrated over the bandwidth of the order-sorting filter. The result is high spatial resolution images of integrated line intensity, observed line wavelength, line width, and underlying continuum flux. Performing these calculations independently at each (α, δ) ensures that all of these quantities are determined accurately over the whole FOV.

3. M82 [Fe II] EMISSION

3.1. Morphology

Figure 3 (Plate 1) (also Fig. 4a [Pl. 2]) is an image of [Fe II] 1.644 μ m integrated line intensity in M82. The prominent K-band (2.2 μ m) continuum sources mapped by Dietz et al. (1986) and the radio sources mapped by Kronberg, Biermann, & Schwab (1985) are plotted on the image for reference. Two general categories of emission are seen: (1) a distributed [Fe II] background emission extending throughout the nuclear region of the galaxy and (2) compact [Fe II] sources at several locations southwest of the nucleus. Compact sources were identified using the task DAOFIND in the DAOPHOT software package in IRAF (Stetson 1987). Six compact sources were identified and are labeled on Figure 4. Their positions, FWHM source diameter, and integrated line flux are listed in Table 1.

There is excellent spatial correspondence between the two unresolved [Fe II] sources in the southwest corner of the image and the Dietz et al. sources K5 and K6. These sources are strong [Fe II] point sources that have not been detected in the radio continuum (e.g., Huang et al. 1994; Muxlow et al. 1994; Carlstrom & Kronberg 1991; Kronberg et al. 1985). A ridge of [Fe II] emission is associated with K5 and extends to K6. The eastern terminus of this ridge corresponds to a point of high foreground extinction mapped by Satyapal et al. (1995), and we suspect that this ridge actually extends eastward along the disk of the galaxy, connecting with the [Fe II] emission seen in the inner 150 pc region of the nucleus (K1) where several compact, spatially resolved [Fe II] sources are seen.

In Table 1, we list observed line fluxes and positions for the prominent [Fe II] sources, and also include Pa β and A_V data from Satyapal et al. (1995). The listed fluxes were spatially integrated over circular regions of diameter equal to the FWHM extent of the sources. We find that K5 and K6 (Fe 5 and Fe 6 in Table 1) exhibit a [Fe II] 1.644/Pa β ratio that is significantly higher than any other [Fe II] source in M82. One would infer a [Fe II] 1.644/B γ ratio of approximately 4, or a [Fe II] 1.257/H β ratio of 0.2 for the source K6.¹⁰ The former value, and the upper limit to the source size imposed by our spatial resolution, suggest that K6 is comparable in size and emission to the brightest [Fe II]

TABLE 2
M82 [Fe II] AND Pa β PHOTOMETRY (10^{-17} W m $^{-2}$) COMPARED WITH OTHER DATA

SOURCE	BEAM (arcsec)	A_V^a	THIS PAPER			PAPER I		LESTER ET AL. ([Fe II] 1.6)
			[Fe II] 1.6	[Fe II] 1.3 ^b	Pa β^c	[Fe II] 1.3	Pa β	
Nucleus	3.8	5.0	13.9	16.0
K2	2.7	6.0	9.63	4.60	3.10	4.60	3.89	...
41.9 + 58.1	2.7	6.0	8.95	4.80	2.85	13.5	5.55	...
44.0 + 59.5	2.7	3.2	8.50	6.50	2.61	23.0	5.11	...

^a Extinction data from Satyapal et al. (1995) averaged over listed aperture.

^b Derived from [Fe II] 1.644 using listed A_V .

^c Pa β data from Satyapal et al. (1995).

sources in NGC 253 (Forbes et al. 1993). The latter value is in agreement with model predictions of [Fe II] 1.257/H β behind 100 km s $^{-1}$ grain-processing shocks (Shull & Draine 1987).

In Table 2, we present [Fe II] and Pa β fluxes at positions and in apertures chosen to facilitate comparison with M82 [Fe II] data published by others. We find generally good correspondence with results reported in Paper I and Lester et al. (1990) on the nucleus and K2. However, we find lower [Fe II] and Pa β fluxes than reported in Paper I on the radio sources 44.0 + 59.5 and 41.9 + 58.1. In Paper I, we assumed that the [Fe II] surface brightness was distributed uniformly within the 2.7 diameter circular aperture of the grating spectrometer. However, these new high spatial resolution Fabry-Perot images reveal that this emission has spatial structure on a smaller scale. As discussed in § 3.3, we find that the [Fe II] fluxes associated with the radio sources 44.0 + 59.5 and 41.9 + 58.1 in Paper I were dominated by compact sources on the periphery of the beam.

One expects the [Fe II] morphology shown in Figure 3 to be affected by nonuniform foreground extinction. Satyapal et al. (1995) derived a foreground-extinction map of M82 from Fabry-Perot images of Br γ and Pa β obtained with the same observing system at the same spatial and spectral resolution as the [Fe II] data presented here. We have used this infrared-extinction map to correct Figure 4a, assuming that no variable extinction exists between the [Fe II] and the H recombination line-emitting regions. Combination of the statistical uncertainty in the A_V and [Fe II] data increases the noise in the resulting corrected image. Those regions where the extinction-corrected [Fe II] flux was determined with $\geq 2 \sigma$ confidence are shown in Figure 4b (Plate 2). Information is lost on the K5 and K6 region of Figure 4b, but a high signal-to-noise ratio remains throughout the inner 150 pc region that contains sources Fe 1–4. The source Fe 4 is revealed with high contrast by this procedure.

One can see that these sources are intrinsically compact and do not result from holes in a foreground-extinction screen. The brightest source is located just west of the nucleus and consists of a 110 pc \times 40 pc emission region elongated along P.A. = 40°, with maximum emission at its southern end and a secondary maximum northwest of this position. We interpret this structure as two sources (Fe 1 and Fe 2, Table 1) that exhibit a FWHM diameter of

roughly 40 pc. Source Fe 4 (Table 1) is 40 pc \times 30 pc FWHM elongated north-south. We note that, if the emission region encompassing Fe 1 and Fe 2 were interpreted as resulting from two adjacent supernova remnants, and if source Fe 4 were due to a single remnant, these remnants would individually be similar in size to the Cygnus Loop (diameter \sim 40 pc, age $\sim 5 \times 10^4$ yr). In contrast, remnants corresponding to the spatially unresolved sources Fe 3, Fe 5, and Fe 6 would have to be at least a factor of 2 smaller and, as a consequence, much younger than the 40 pc sources.

We note that no strong spatial correlation exists between the [Fe II] sources and the [Ne II], [Ar III], [S IV], and Br α sources mapped by Achtermann & Lacy (1995, hereafter AL95). The sources Fe 2 and Fe 3 lie roughly 15 pc north of the AL95 sources W1 and W2. We find no [Fe II] counterpart to the AL95 source E1, and no evidence for local maxima in the [Ne II] surface brightness at the position of Fe 1, Fe 4, Fe 5, or Fe 6 is apparent in the AL95 line maps. This noncorrelation is not surprising due to the factor of 3 difference in ionization potential between photo-dissociation region (PDR) species, such as Fe $^+$, and the H II region species, such as [Ne II], although the latter is also modeled to trace fast shocks (e.g., Shull & Draine 1987). We also note that no [Fe II] source was found at the position of the [Ni II] source reported by Rank et al. (1995).

Figure 4c (Plate 2) is a composite image consisting of [Fe II] data shown in Figure 4a (red) and Br γ data from Satyapal et al. (1995) (green). Yellow is a mixture of these components. One can see that the distributed [Fe II] emission is extended to the south relative to Br γ in the general direction of the galaxy's minor axis. This extended emission accounts for 90% of M82's [Fe II] luminosity (Table 3). A similar morphology has been seen in NGC 4945 (Moorwood & Oliva 1994) in which [Fe II] 1.644 μ m is extended symmetrically along the minor axis relative to Br γ . However, in M82, the [Fe II] emission is very asymmetric, with no extension to the north relative to Br γ , and no compact [Fe II] sources east or north of the nucleus are seen. This asymmetry is not seen in the 1.64 μ m continuum.

TABLE 3
M82 [Fe II] 1.644 μ m LUMINOSITIES^a

Region	Observed	Extinction Corrected
30" diameter field	0.55	1.20
Total of compact sources	0.03	0.14
Total extended emission	0.52	1.06

^a 10^{40} ergs s $^{-1}$, $d = 3.2$ Mpc.

¹⁰ We note that [Fe II] 1.257/[Fe II] 1.644 = 1.36 (no extinction), $j_{H\beta/Pa\beta} = 6.1$, and $j_{Pa\beta/Br\gamma} = 5.7$ (case B, 10^4 K; Hummer & Story 1987), and we caution that significant departures from case B predictions for $I_{Br\gamma}/I_{H\beta}$ are often seen in supernova remnants and galactic nuclei (e.g., Oliva, Moorwood, & Danziger 1989; Moorwood 1989).

Hence, foreground extinction to the northern half of the disk is not a possible explanation. We note that this north-south asymmetry is also seen in the X-ray continuum (Bregman, Schulman, & Tomisaka 1995) and in the distribution of 6 cm radio continuum point sources (Muxlow et al. 1994).

This asymmetric [Fe II] spatial distribution most likely traces low iron depletion gas from the galactic disk that has been entrained in a supernova-driven wind. The north-south asymmetry suggests that the wind has broken out of the disk in a southerly direction only. One could also speculate that the asymmetric morphology of this outflow and the southern concentration of supernova remnants are related to the H I stream that extends south from M82 and bridges the M81/M82 system (e.g., Gottesman & Welia-chew 1977; Yun, Ho, & Lo 1993).

3.2. Iron Depletion in M82

The gas-phase abundance of Fe⁺ can be derived from our measured [Fe II]/Pa β ratios as

$$\frac{N(\text{Fe}^+)}{N(\text{H})} \sim 9 \times 10^{-6} \frac{I([\text{Fe II}]1.644)}{I(\text{Pa}\beta)} \quad (1)$$

(e.g., van der Werf et al. 1993), where we have assumed a volume emission coefficient for Pa β of $j_{\text{Pa}\beta}/n_e^2 = 2.42 \times 10^{-27}$ ergs s⁻¹ cm⁻³ sr⁻¹ for case B recombination at $T = 10^4$ K (Table 4.2 in Osterbrock 1974). We assume low density ($n_e \leq 10^4$ cm⁻³) for the [Fe II]-emitting regions such that the $a^4 D$ term of Fe⁺ is not thermalized (Paper I), and we take $N(\text{Fe}^+)/N(\text{Fe})$ as order unity in shock recombination zones (Paper I).

From equation (1) and Table 1, we find a gas-phase iron abundance $N(\text{Fe})/N(\text{Fe})_\odot \geq 0.04$ averaged over sources Fe 1–4, and on sources Fe 5 and Fe 6, we find $N(\text{Fe})/N(\text{Fe})_\odot \geq 0.12$. For M82 as a whole (30" diameter field), we find $L_{[\text{Fe II}]} = 5.5 \times 10^{39}$ ergs s⁻¹ (Table 3) and $L_{\text{Br}\gamma} = 6.5 \times 10^{39}$ ergs s⁻¹ (Satyapal et al. 1995) yielding a global gas-phase abundance of $N(\text{Fe})/N(\text{Fe})_\odot \geq 0.16$. The lower limits derive from our assumption that all of the iron is singly ionized. These data show that the iron depletion in these sources is at least an order of magnitude lower than typical interstellar values along reddened lines of sight in the Galactic interstellar medium (de Boer, Jura, & Shull 1987), and is at most roughly equivalent to model predictions of iron depletion behind moderate-density 100 km s⁻¹ shocks (McKee, Chernoff, & Hollenbach 1984), consistent with the idea that the [Fe II] morphology in M82 traces regions of grain destruction (Paper I). We note that the global $L_{[\text{Fe II}]} / L_{\text{Br}\gamma}$ ratio we derive is consistent with radio supernovae models of Colina (1993) that involve a Salpeter ($\alpha = 2.35$) initial mass function slope with an upper mass limit of 25 M_\odot . However, $L_{[\text{Fe II}]}$ and $L_{\text{Br}\gamma}$ are individually a factor of 2 in excess of this prediction. The compact morphology of M82's [Fe II] sources strongly suggests that these sources are supernova remnants. However, at the high spatial resolution of these new data, we find that these sources are distinct from the population of radio point sources revealed on 6 cm radiographs of M82.

3.3. [Fe II] and Radio Continuum Sources

In Paper I, we obtained [Fe II] 1.257 spectra, with a spatial resolution of 42 pc, of two nonthermal 6 cm continuum sources, 41.9 + 58.1 and 44.0 + 59.5 (Kronberg et al. 1985), and a K-band continuum source K2 (Dietz et al. 1986). We compared the [Fe II] emission of the radio

sources with K2, and also with archival [Fe II] data on K1 reported by Lester et al. (1990). We concluded that the [Fe II] surface brightness had local maxima at the position of these two radio sources. At the higher spatial resolution (20 pc) of the new data reported here (Fig. 4), we find that the [Fe II] source previously attributed to 44.0 + 59.5 is displaced one spatial resolution element south of this radio source. We also find that the [Fe II] emission attributed to 41.9 + 58.1 is due to emission on the northeast and southwest periphery of the 2"7 beam used in our past measurements (Paper I), such that the [Fe II] emission at this position is actually attributed to sources Fe 2 and Fe 4 rather than to the radio source.

Although several of the [Fe II] sources in Table 1 are in close proximity to one or more radio continuum sources, we find no strong spatial correlation between the [Fe II] and the radio continuum sources mapped by Kronberg et al. (1985) or more recently by Muxlow et al. (1994). In terms of total spatially integrated luminosity, [Fe II] and 6 cm emission components are tightly correlated (e.g., Forbes & Ward 1994). However, in terms of spatial morphology, these components are not correlated. Since the [Fe II] point sources make only a small direct contribution to the total [Fe II] luminosity at these wavelengths (Table 3), we conclude that this luminosity correlation is tracing the distributed components. The lack of spatial correlation between the [Fe II] and radio point sources and the size of the spatially resolved [Fe II] sources suggests that these components are tracing separate populations of supernova remnants that differ significantly in age.

The radio point sources in M82 are interpreted as young supernova remnants rather than radio supernovae, based on the temporal development of their 6 cm flux. Many of these remnants have been spatially resolved. Their age is constrained by their size. Muxlow et al. (1994) report 2.4 pc as a mean remnant diameter for the population and derive a corresponding mean age of ~ 200 yr assuming preadiabatic expansion at 5000 km s⁻¹. In contrast, we find that the [Fe II] sources are typically a factor of 20 larger than the 6 cm sources. The proportionality between remnant diameter and age $r \propto t^n$ changes as the remnant evolves through free expansion ($n = 1$), adiabatic ($n = \frac{2}{5}$), and radiative ($n = \frac{1}{4}$) phases of expansion (e.g., Spitzer 1978). We note that the size contrast between the [Fe II] and the 6 cm remnants in M82 is similar to that exhibited by the Cygnus Loop (age 5000 yr) and Cas A (age 300 yr). A natural interpretation for the compact [Fe II] sources in M82 is that they trace a population of supernova remnants that are at least an order of magnitude older than those observed in the radio continuum. We note that the size distribution of the [Fe II] sources spans at least a factor of 2. Assuming that these remnants are in radiative expansion, they must span a factor of 10–20 in age. Hence, these data suggest that [Fe II] remains an important coolant in supernova remnants for at least 10^3 yr after outburst. We note that [Fe II] emission associated with the 2 pc radio sources would be diluted by our 20 pc seeing-limited resolution. As a consequence, the [Fe II] background emission observed throughout the nuclear region could possibly inhibit their detection. Similarly, 6 cm emission associated with the bright 20–40 pc [Fe II] sources would be difficult to detect against the 6 cm continuum background (T. W. B. Muxlow 1996, private communication). However, we note that the sources Fe 5 and Fe 6 would be good candidates to search for a radio

continuum counterpart since they are the most compact [Fe II] sources and occur at a location where the 6 cm continuum background is a minimum.

We find that the [Fe II] luminosity of the sources listed in Table 1 exceeds that expected in Galactic or LMC supernova remnants (10^{33} – 10^{36} ergs s^{-1} ; Oliva et al. 1989) by factors ranging from 1 to several orders of magnitude. A similar affect was noted by Kronberg et al. (1985), who reported 6 cm compact source luminosities that exceed Cas A by 2 orders of magnitude. Averaging over observed data listed in Table 1, we estimate the typical [Fe II] luminosity of a M82 supernova remnant as at least 10^{38} ergs s^{-1} (cf. Colina 1993). Assuming that this emission remains roughly constant as the remnant ages, we find that the total [Fe II] luminosity of M82 can be accounted for by roughly 10^2 supernova remnants. If their [Fe II] emission persists for 10^3 yr, then these data would suggest a supernova rate of at most 0.1 yr^{-1} , consistent with that derived by Van Buren & Greenhouse (1994) from radio data on M82.

3.4. [Fe II] and Photospheric Continuum Emission

If the [Fe II]/Br γ flux ratio is tracing the relative contribution of supernova remnants and Lyman continuum-producing stars within a stellar cluster, then these data can yield a general age indicator of the central starburst in M82 (Paper I). At the onset of a starburst, the stellar population should be characterized by a large H recombination line luminosity, a small [Fe II] luminosity, and blue near-infrared continuum colors. As the most massive stars formed during the burst evolve off the main sequence, the [Fe II] luminosity will increase with the supernova rate, emission from low-depletion PDRs will increase relative to H II regions, and the photospheric continuum will become redder.

We find a correlation between the $J-H$ color and the extinction-corrected [Fe II]/Br γ flux ratio within the central 500 pc of M82 (Fig. 5). The J and H broadband data shown in Figure 5 have been corrected for extinction and free-free and free-bound continuum emission. We find that dust emission and our measured Pa β and [Fe II] line fluxes have a negligible effect on the $J-H$ color of M82 (see Satyapal et al. 1995, 1996). As a result, we assume that the corrected

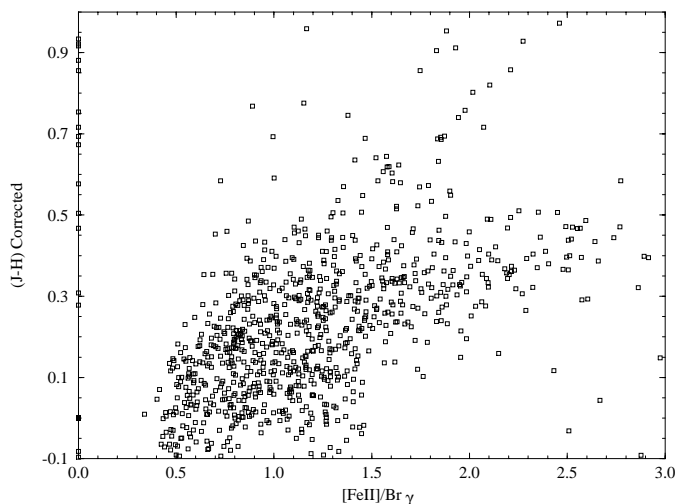


FIG. 5.—The $J-H$ color of photospheric continuum emission vs. [Fe II] 1.644/Br γ line ratio within the central 500 pc of M82.

color shown in Figure 5 reliably traces direct photospheric emission from M82's stars (cf. Koornneef 1983). We find that the [Fe II]/Br γ line ratio throughout M82 correlates with the age of the starburst as reflected by the color of photospheric emission from the galaxy's stars. This correlation suggests that the [Fe II] emission regions in M82 are colocated with the post-main-sequence stellar population, and lends credence to the idea that infrared [Fe II]/H II line ratios can yield a relative age-dating technique for starburst clusters.

3.5. The [Fe II] Rotation Curve of M82

Although the resolving power of our Fabry-Perot etalons is $\approx 375 \text{ km s}^{-1}$, our data reduction algorithms (§ 2.2) enable systemic velocity measurements to be made with a precision of approximately 40 km s^{-1} across the whole FOV. As a consequence, we easily resolve the rotation of M82. The relative [Fe II] emission-line velocity along the major axis of the galaxy is shown in Figure 6. Good agreement is found between our [Fe II] rotation curve and those derived from H α measurements (Gotz et al. 1990). In addition, our velocity gradient is in close agreement with [S III] 9069 Å measurements by McKeith et al. (1993). This agreement provides confirmation that our Fabry-Perot observation and data reduction techniques (§ 2.2) are accurate over the whole FOV shown in Figure 4.

3.6. Conclusions

We conclude that infrared Fabry-Perot imaging is a powerful technique for high spatial resolution imaging spectroscopy in applications requiring high spectral purity relative to circular variable filter imaging, and wide fields relative to those obtained by integral field slit spectrometers. Our [Fe II] Fabry-Perot images of M82 have revealed a population of supernova remnants that are substantially older than those revealed on 6 cm radiographs of similar spatial resolution. We note that this interpretation, combined with recent evidence for radially propagating starburst activity in M82 (e.g., Satyapal et al. 1996), would imply that the [Fe II] sources should be more centrally concentrated than the 6 cm sources. This expectation is consistent with observation.

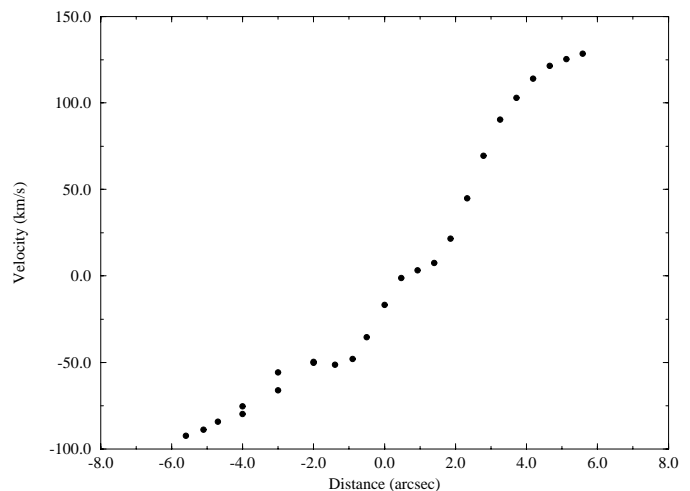


FIG. 6.—The [Fe II] 1.644 μm rotation curve along the major axis of M82. The distance is shown relative to the nucleus, and the velocity was derived from the line wavelength measured relative to the nucleus along P.A. 120° .

We also find that the nuclear region of M82 contains a distributed [Fe II] background emission that accounts for 90% the galaxy's [Fe II] luminosity and traces a region where the gas-phase abundance of iron is at least 16% of solar. We find that the gas-phase iron abundance correlates spatially with the color temperature of the photospheric continuum, suggesting that the low iron depletion regions are associated with evolved stars rather than H II regions.

Among the most interesting aspects of M82's [Fe II] morphology is its asymmetry. We find that the minor-axis extension of the [Fe II] emission follows the north-south asymmetry revealed in *ROSAT* HRI continuum maps, and no compact [Fe II] sources were detected east or north of the nucleus where a [Ni II] source was recently observed from the Kuiper Airborne Observatory. Indeed, at 20 pc resolution, we find no [Fe II] compact sources in spatial coincidence with young (2 pc diameter) supernova remnants. Similarly, no 6 cm sources of sizes comparable to the [Fe II] sources (20–40 pc diameter) have been detected.

3.7. Starburst Fossil Remnants

Can poststarburst galaxies be distinguished from normal galaxies? If the distributed [Fe II] emission observed along

the minor axis of M82 and NGC 4945 is tracing low-depletion disk material entrained in a starburst super wind, then after the cessation of starburst activity, this material should, in many cases, occupy a halo surrounding the galaxy. If the low-depletion state of this gas were persistent in the halo environment, then it could provide an observable fossil remnant of the starburst. One could perhaps image poststarburst low-depletion halos via low-excitation, potential ground-state, fine-structure transitions of refractory ions using the Stratospheric Observatory For Infrared Astronomy (SOFIA). Examples would include the $a^6D(7/2-9/2)$ transition of [Fe II] near $26\ \mu\text{m}$ and the $a^5D(3-4)$ transition of [Fe III] near $23\ \mu\text{m}$. Both transitions have low-excitation potential (550 and 628 K, respectively) and would be excited in a quiescent poststarburst environment.

We thank T. Heckman and T. Muxlow for comments and data in advance of publication. We also thank John Lacy for comments as referee. This work was supported in part by the Smithsonian Institution Scholarly Studies Program, NASA grant NAGW1711, NSF grants AST 94-53354 and AST 93-57392, and the Office of Naval Research.

REFERENCES

- Achtermann, J. M., & Lacy, J. H. 1995, *ApJ*, 439, 163 (AL95)
 Atherton, P. D., Reay, K. N., Ring, J., & Hicks, T. R. 1981, *Opt. Eng.*, 20, 806
 Blietz, M., Cameron, M., Drapatz, S., Genzel, R., Krabbe, A., van der Werf, P., Sternberg, A., & Ward, M. 1994, *ApJ*, 421, 92
 Bregman, J. N., Schulman, E., & Tomisaka, K. 1995, *ApJ*, 439, 155
 Carlstrom, J. E., & Kronberg, P. P. 1991, *ApJ*, 366, 422
 Colina, L. 1993, *ApJ*, 411, 565
 de Boer, K. S., Jura, M. A., & Shull, M. J. 1987, in *Accomplishments of the IUE*, ed. Y. Kondo (Dordrecht: Reidel), 485
 Dietz, R. D., Smith, J., Hackwell, J. A., Gehr, R. D., & Grasdalen, G. L. 1986, *AJ*, 91, 758
 Forbes, D. A., & Ward, M. J. 1993, *ApJ*, 416, 150
 ———. 1994, in *ASP Conf. Ser. 54, The First Stromlo Symposium: The Physics of Active Galaxies*, ed. G. V. Bicknell, M. A. Dopita, & P. J. Quinn (San Francisco: ASP), 429
 Forbes, D. A., Ward, M. J., Rotaciuc, V., Blietz, M., Genzel, R., Drapatz, S., van der Werf, P. P., & Krabbe, A. 1993, *ApJ*, 406, L11
 Grevesse, N., & Anders, E. 1989, in *Cosmic Abundances of Matter*, ed. C. J. Waddington (New York: AIP), 1
 Gottesman, S. T., & Weliachew, L. 1977, *ApJ*, 211, 47
 Gotz, M., McKeith, C. D., Downes, D., & Greve, A. 1990, *ApJ*, 240, 52
 Greenhouse, M. A., Woodward, C. E., Thronson, H. A., Rudy, R. J., Rossano, G. S., & Erwin, P. 1991, *ApJ*, 383, 164 (Paper I)
 Huang, Z. P., Thuan, T. X., Chevalier, R. A., Condon, J. J., & Yin, Q. F. 1994, *ApJ*, 424, 114
 Hummer, D. G., & Storey, P. J. 1987, *MNRAS*, 224, 801
 Koornneef, J. 1983, *A&A*, 128, 84
 Kronberg, P. P., Biermann, P., & Schwab, F. R. 1985, *ApJ*, 291, 693
 Lester, D. F., Carr, J. S., Joy, M., & Gaffney, N. 1990, *ApJ*, 352, 544
 Lumsden, S. L., & Puxley, P. J. 1995, *MNRAS*, 276, 723
 McKee, C. F., Chernoff, D. F., & Hollenbach, D. J. 1984, in *Galactic and Extragalactic Infrared Spectroscopy*, ed. M. F. Kessler & J. P. Phillips (Dordrecht: Reidel), 103
 McKeith, C. D., Castles, J., Greve, A., & Downes, D. 1993, *ApJ*, 272, 98
 Moorwood, A. F. M. 1989, in *Proc. 22d ESLAB Symposium on Infrared Spectroscopy in Astronomy*, ed. B. H. Kaldeich (Paris: ESA), 507
 Moorwood, A. F. M., & Oliva, E. 1994, *ApJ*, 429, 602
 Mouri, H., Kawara, K., & Taniguchi, Y. 1993, *ApJ*, 406, 52
 Muxlow, T. W. B., Pedlar, A., Wilkinson, P. N., Axon, D. J., Sanders, E. M., & de Bruyn, A. G. 1994, *MNRAS*, 266, 455
 Nahar, S. N. 1995, *A&A*, 293, 967
 Oliva, E., Moorwood, A. F. M., & Danziger, I. J. 1989, *A&A*, 214, 307
 Osterbrock, D. E. 1974, *Astrophysics of Gaseous Nebulae* (San Francisco: Freeman)
 Pipher, J. L., Moneti, A., Forrest, W. J., Woodward, C. E., & Shure, M. A. 1987, in *Proc. Workshop on Ground-based Astronomical Observations with Infrared Detectors*, ed. C. G. Wynn-Williams & E. E. Becklin (Honolulu: IfA), 326
 Pradhan, A. K., & Zhang, H. L. 1993, *ApJ*, 409, L77
 Rank, D., Temi, P., Bregman, J., Dunham, E., & Harker, D. 1995, in *ASP Conf. Ser. 73, Airborne Astronomy Symposium on the Galactic Ecosystem*, ed. M. R. Hass, J. A. Davidson, & E. F. Erickson (San Francisco: ASP), 437
 Satyapal, S., et al. 1995, *ApJ*, 448, 611
 Satyapal, S., Watson, D. M., Pipher, J. L., Forrest, W. J., Greenhouse, M. A., Smith, H. A., Fischer, J., & Woodward, C. E. 1996, *ApJ*, submitted
 Schroeder, D. J. 1987, *Astronomical Optics* (New York: Academic), 19
 Shull, J. M., & Draine, B. T. 1987, in *Interstellar Processes*, ed. D. J. Hollenbach & H. A. Thronson (Dordrecht: Reidel), 283
 Spitzer, L. 1978, *Physical Processes in the Interstellar Medium* (New York: Wiley)
 Stetson, P. B. 1987, *PASP*, 99, 191
 Tammann, G. A., & Sandage, A. 1968, *ApJ*, 151, 825
 Van Buren, D., & Greenhouse, M. A. 1994, *ApJ*, 431, 640
 van der Werf, P. P., Genzel, R., Krabbe, A., Blietz, M., Lutz, D., Drapatz, S., Ward, M. J., & Forbes, D. A. 1993, *ApJ*, 405, 522
 Vaughan, J. M. 1989, *The Fabry-Perot Interferometer* (Philadelphia: Adam Hilger)
 Yun, M. S., Ho, P. T. P., & Lo, K. Y. 1993, *ApJ*, 411, L17
 Zhang, H. L., & Pradhan, A. K. 1995, *A&A*, 293, 953

ERRATUM

In the paper “Infrared Fabry-Perot Imaging of M82 [Fe II] Emission. II. Tracing Extragalactic Supernova Remnants” by Matthew A. Greenhouse, Shobita Satyapal, Charles E. Woodward, J. Fischer, K. L. Thompson, W. J. Forrest, J. L. Pipher, N. Raines, H. A. Smith, D. M. Watson, and R. J. Rudy (ApJ, 476, 105 [1997]), there are errors in Figure 4 (Plate 2) and Table 1. In Figure 4, the panels of the plate were mislabeled by the printer. As the plate appears, the top panel is actually Figure 4c and the bottom panel is actually Figure 4a. In Table 1, diameters given in the fifth column, for the unresolved sources Fe 3, Fe 5, and Fe 6 should appear as “<22” rather than “22”.